Front. Energy 2021, 15(3): 721–731
https://doi.org/10.1007/s11708-021-0766-8

RESEARCH ARTICLE

Dong LIU*, Zhuqing YAN*, Peng ZENG, Haoran LIU, Tianyou PENG, Renjie LI

In situ grown TiN/N-TiO_2 composite for enhanced photocatalytic H_2 evolution activity

Abstract Titanium nitride (TiN) decorated N-doped titania (N-TiO_2) composite (TiN/N-TiO_2) is fabricated via an *in situ* nitridation using a hydrothermally synthesized TiO_2 and melamine (MA) as raw materials. After the optimization of the reaction condition, the resultant TiN/N-TiO_2 composite delivers a hydrogen evolution activity of up to 703 μmol/h under the full spectrum irradiation of Xe-lamp, which is approximately 2.6 and 32.0 times more than that of TiO_2 and TiN alone, respectively. To explore the underlying photocatalytic mechanism, the crystal phase, morphology, light absorption, energy band structure, element composition, and electrochemical behavior of the composite material are characterized and analyzed. The results indicate that the superior activity is mainly caused by the *in situ* formation of plasmonic TiN and N-TiO_2 with intimate interface contact, which not only extends the spectral response range, but also accelerates the transfer and separation of the photoexcited hot charge carrier of TiN. The present study provides a fascinating approach to *in situ* forming nonmetallic plasmonic material/N-doped TiO_2 composite photocatalysts for high-efficiency water splitting.

Keywords photocatalytic H_2 evolution, TiN/N-TiO_2 composite, plasmonic effect, *in-situ* nitridation

Received Feb. 4, 2021; accepted Apr. 27, 2021; online Jul. 30, 2021

Dong LIU, Peng ZENG (✉)
Research Institute of Wuhan University in Shenzhen, Shenzhen 518057, China
E-mail: boriszeng@hotmail.com

Zhuqing YAN, Haoran LIU, Renjie LI (✉)
College of Chemistry and Molecular Sciences, Wuhan University, Wuhan 430072, China
E-mail: lirj@whu.edu.cn

Tianyou PENG (✉)
Research Institute of Wuhan University in Shenzhen, Shenzhen 518057, China; College of Chemistry and Molecular Sciences, Wuhan University, Wuhan 430072, China
E-mail: typeng@whu.edu.cn

*These authors contributed to this work equally.

Special Issue—Photocatalysis: From Solar Light to Hydrogen Energy (Guest editors: Wenfeng SHANGGUAN, Akihiko KUDO, Zhi JIANG, Yuichi YAMAGUCHI)

1 Introduction

Since the water splitting over a titania (TiO_2) photoelectrode was reported for the first time [1], photocatalytic hydrogen (H_2) production employing semiconducting photocatalysts has been considered as a promising and fascinating method to alleviate the current energy shortage [2–5]. Of various photocatalysts developed, TiO_2 as an n-type semiconductor is the most extensively explored one owing to its merits of environmentally friendliness, low cost, and robust physicochemical stability. Nevertheless, TiO_2 with a wide bandgap (approximately 3.20 eV) can only absorb the UV light in the solar spectrum, while the UV ray ($\lambda < 400$ nm) just accounts for a small part (approximately 4%) of the solar spectrum [5]. To effectively utilize the approximately 53% of visible light and even approximately 43% of infrared rays in solar light and improve the photocatalytic performance, enormous approaches, such as doping with extra elements [6,7], exploiting narrow bandgap semiconductors [2,3], constructing semiconducting composites [7–12], and dye-sensitization systems [5,13], have been explored, of which, the construction of semiconductor-based heterojunctions is an efficient strategy to elevate the light capturing ability and to retard the photoexcited charge recombination at the same time, therefore making it attractive and challenging topic in the field of photocatalytic energy conversion [6–17].

Titanium nitride (TiN) with a typical face-centered cubic (fcc) structure has been extensively applied in the field of electrochemical energy conversion due to its excellent metallic characteristics and physicochemical stability [18–20]. In addition, TiN possesses a good plasmonic effect,

even similar to gold, in the visible light and near-infrared (NIR) spectral range [20–22], and its work function (approximately 4.0 eV versus vacuum) is larger or equal to the electron affinity of most metal oxide semiconductors used in the field of photocatalysis [23], and thus it is expected to construct favorable energetic alignment for hot carrier-improved photocatalytic performance [21]. This inspires researchers to integrate the nonmetallic plasmonic TiN with TiO_2 to attain synergistic benefits of efficient visible light capturing and electric conductivity for enhancing the photocatalytic energy conversion. Although there are some reports on plasmonic TiN boosting the photoelectrochemical oxygen evolution reaction [20,21], the application of TiN in photocatalytic H_2 evolution reaction has not been reported to the best of the authors' knowledge.

Herein, TiN was obtained via a facile and environmentally friendly nitridation process using a hydrothermally synthesized TiO_2 and melamine (MA) as raw materials, whereby TiN was *in situ* grown on the formed N-doped TiO_2 (N-TiO_2), which was confirmed by a series of material characterization and analysis methods. By varying the TiO_2/MA mass ratio, various TiN/N-TiO_2 composites were synthesized. Under light irradiation, the photoinduced hot charge carriers can separate and transfer via the close contact interface of TiN/N-TiO_2 composite, restraining the charge recombination, and the *in situ* formed plasmonic TiN and N-TiO_2 can extend the spectral response range of TiO_2 and promote the transfer and separation of the hot charge carrier of TiN. Therefore, a high H_2 evolution activity was realized. In addition, the energy band structure and electrochemical behavior were investigated to probe the underlying photocatalytic mechanism.

2 Experimental

2.1 Material preparation

TiN/N-TiO_2 composite was prepared via a two-step process, whereby TiO_2 was pre-synthesized via a hydrothermal and calcination processes similar to the previously reported method [24]. Then the hydrothermally synthesized TiO_2 was mixed with melamine (MA). After grinded evenly, the mixture was calcined at 750°C for 2 h in a tube furnace at a N_2 flow of 50 mL/min. The resulting product was washed with ethanol and distilled water serval times, and dried at 100°C overnight to obtain the TiN/N-TiO_2 composite.

For comparison, various composites were fabricated in a similar *in situ* nitridation process of the hydrothermally synthesized TiO_2 by varying the TiO_2/MA mass ratio to 1:5, 1:7, and 1:10, and the corresponding product was denoted as TiN/N-TiO_2-5, TiN/N-TiO_2-7, and TiN/N-TiO_2-10, respectively. Moreover, a pure phase TiN product was prepared by enhancing the TiO_2/MA mass ratio to 1:20 and denoted as TiN. In addition, the hydrothermally synthesized TiO_2 was calcined at 750°C for 2 h in a tube furnace at N_2 flow but without MA, and the relative sample was denoted as TiO_2(c).

2.2 Material characterization

A Miniflex 600 X-ray diffractometer (XRD) with CuKα radiation (λ = 1.54184 Å) was applied to acquire the crystal structure of the sample operated at 40 kV, 15 mA and a scanning rate of 8 °/min with a step of 0.02°. A Zeiss-Sigma field emission scanning electron microscope (FESEM) and a Laboratory$_6$ JEM-2100 (HR) high-resolution transmission electron microscope (HRTEM) working at 200 kV were employed to observe the morphology and microstructure. A field-emission electron probe microanalyzer (EMPA) was applied to quantitatively analyze the contents of Ti, O, N, and C elements. X-ray photoelectron spectroscopy (XPS) measurement was performed on an ESCALAB 250 Xi photoelectron spectroscope (Thermo Fisher Co.) equipped with a standard and monochromatic source (Al Kα), and the binding energy was calibrated by C1s peak (284.6 eV). A Shimadzu UV-3600 spectrophotometer equipped with an integrating sphere was used to obtain the UV-vis diffuse reflectance absorption spectrum (DRS) with $BaSO_4$ as the reference.

The transient photocurrent response of the product was recorded on a CHI Model 618 C electrochemical workstation at a bias potential of 0.5 V using a typical three-electrode system, in which the Pt plate, the Pt wire, and the saturated calomel electrode (SCE) acted as the working electrode, the counter electrode, and the reference electrode, respectively. Typically, 20 mg of photocatalyst was dispersed in the Na_2SO_4 aqueous solution (1.0 mol/L). Before irradiation, the suspension was bubbled with the N_2 flow for 0.5 h to eliminate the residual air. The electrochemical impedance spectrum (EIS) was measured over the frequency range of 0.01–10000 Hz using a three-electrode system, in which the Pt wire and the SCE electrode were used as the counter electrode and the reference electrode, respectively. The working electrode was prepared by depositing photocatalyst suspension containing Nafion and ethanol (0.20 mL, 2.5 g/L) on a fluorine-doped tin oxide (FTO) glass (1.0 cm^{-2}), which was heated at 60°C for 1.0 h to volatilize the solvent and steady the sample. In a typical run, the above three electrodes were immersed into a Na_2SO_4 solution (1.0 mol/L), which was continuously purged by the N_2 flow for 30 min before irradiation.

The flat-band potential (E_{fb}) of the sample was measured using the same three-electrode system as the EIS spectrum. E_{fb} is estimated by extrapolating each Mott-Schottky plot to the *x*-axis to obtain the intercept following Eq. (1) [25],

$$C^{-2} = [2/(e\varepsilon\varepsilon_0 N_d)](V_a - E_{fb} - KT/e), \quad (1)$$

where C is the capacitance of the space charge layer, N_d is the number of donors and estimated by the slope of Eq. (1), e is the electron charge (1.602×10^{-19} C), ε is the dielectric constant, ε_0 is the vacuum permittivity (8.85×10^{-14} F/cm), and K is the Boltzmann constant (1.38×10^{-23} J/K).

2.3 Photocatalytic performance measurement

The photocatalytic H_2 evolution reaction was performed in a top-irradiated Pyrex glass reaction cell [26,27]. Typically, 30 mg of photocatalyst was suspended in a 50 mL of ascorbic acid (AA) solution (50 mmol/L), which was ultrasonically treated for 5 min, vacuumed thoroughly, and then exposed to the full spectrum or visible light ($\lambda > 400$ nm) of a 300 W Xe-lamp (PLS-SXE, Beijing Perfectlight Co. Ltd.) under continuous stirring. The evolved H_2 amount was analyzed by an online SP-6890 gas chromatograph (GC, TCD detector, 5 Å molecular sieve columns, and Ar as carrier gas).

3 Results and discussion

3.1 Microstructure and composition analyses

Figure 1(a) presents the X-ray diffraction (XRD) patterns of the products derived from various TiO_2/MA mass ratios. As seen, the TiO_2(c) product obtained by calcining the hydrothermally synthesized TiO_2 in the absence of MA is still TiO_2 containing anatase and rutile phases, whereby the obvious diffraction peaks at 2θ = 25.3°, 37.8°, 48.0°, 53.9°, 55.1°, and 62.7° can be ascribed to the (101), (004), (200), (105), (211), and (204) plane reflections of anatase TiO_2 (JCPDS No. 21-1272) [25,28], respectively. The additional diffraction peaks at 2θ = 27.4°, 36.1°, 41.2°, and 54.3° can be attributed to the (110), (101), (111), and (211) plane reflections of rutile TiO_2 (JCPDS No. 21-1276) [28,29], respectively. However, there is not any diffraction peak of anatase or rutile phase when the TiO_2 to MA mass ratio is 1:20, and some new weak peaks are observed at 2θ = 36.8°, 42.8°, and 62.1°, which can be attributed to the (111), (200), and (220) plane reflections of face-centered cubic (fcc) TiN [18–20], respectively. This means that the hydrothermally synthesized TiO_2 can be transformed into pure phase TiN, while the weak and broad diffraction peaks imply that the formed TiN has a moderate crystallinity.

When the TiO_2 to MA mass ratio is enhanced to 1:5, 1:7, and 1:10, the corresponding products (TiN/N-TiO_2-5, TiN/N-TiO_2-7, and TiN/N-TiO_2-10) still display the diffraction peaks of anatase TiO_2, while those rutile peaks disappeared. Moreover, new peaks can be observed at 2θ = 36.8°, 42.8°, and 62.1°, which can be attributed to the (111), (200), and (220) plane reflections of fcc TiN [19,20], respectively. Besides, the diffraction peak intensities of anatase TiO_2 decrease gradually, while those of TiN increase upon enhancing the MA addition amount, and those diffraction peaks such as (101) and (200) of anatase TiO_2 slightly shift toward a higher 2θ angle (Fig. 1(b)), which might be ascribed to the substitution of O^{2-} ions (with a radius of 1.40 Å) with N^{3-} ones (with a radius of 1.46 Å) to form N-doped TiO_2 (N-TiO_2) [20]. These results demonstrate that N-TiO_2 and TiN as well as their composites (TiN/N-TiO_2) can be obtained by varying the TiO_2 to MA mass ratio during the *in situ* nitridation process of the hydrothermally synthesized TiO_2.

X-ray photoelectron spectroscopy (XPS) was performed to further explore the component and its surface chemical states of the products. The survey XPS spectra (Fig. 2(a)) suggest that the TiO_2(c) product only contains Ti and O elements in addition to C1s, while the TiN obtained from the TiO_2 to MA mass ratio of 1:20 is mainly composed by

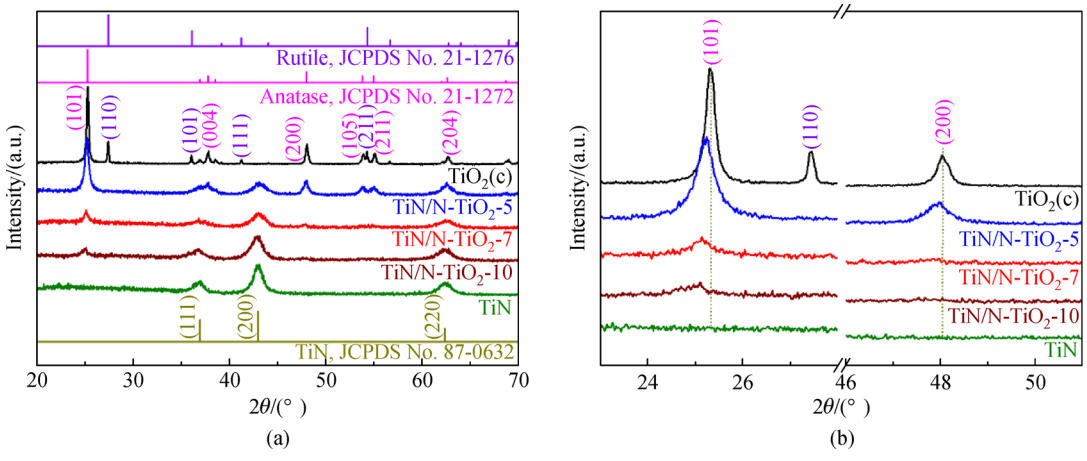

Fig. 1 XRD patterns.

(a) TiO_2(c), TiN, and composites (TiN/N-TiO_2-5, TiN/N-TiO_2-7, and TiN/N-TiO_2-10) derived from different TiO_2/MA mass ratios; (b) local enlarged view in the range of 2θ = 23°–28° and 46°–51°.

Ti and N elements with very weak O 1s and C 1s peaks, indicating the formation of TiN, which is consistent with the above XRD result. As for the TiN/N-TiO_2-7, there exist Ti, O, N, and C element signals in the survey spectrum, manifesting the existence of TiN and TiO_2 (or N-TiO_2). The high-resolution Ti 2p XPS spectrum (Fig. 2(b)) indicates that the TiO_2(c) product exhibits a typical double peak with binding energy (BE) located at 458.6 (Ti $2p_{3/2}$) and 464.3 (Ti $2p_{1/2}$) eV, suggesting the valence state of Ti is + 4 [20,30], while the TiN product derived from the TiO_2 to MA mass ratio of 1:20 displays two BE peaks at 457.9 (Ti $2p_{3/2}$) and 463.6 (Ti $2p_{1/2}$) eV, denoting that the Ti valence state is + 3 [31,32]. In contrast, the Ti 2p spectrum (Fig. 2b) of the TiN/N-TiO_2-7 composite can be deconvolved into three kinds of BE peaks located at 458.9/464.6 eV for the Ti–O bond, 457.5/463.2 eV for the Ti–N bond, and 458.3/464.0 eV for the Ti–N–O bond [20], indicating the coexistence of TiN and N-TiO_2 in the composite.

The high-resolution O 1s XPS spectrum (Fig. 2(c)) demonstrates that the TiO_2(c) product has two main BE peaks at 529.8 and 532.1 eV, which can be attributed to the lattice oxygen atoms of TiO_2 and the surface hydroxyl groups (–OH), respectively. The TiN/N-TiO_2-7 composite displays two similar BE peaks at 530.0 eV and 532.1 eV. The BE peak at 532.1 eV for both TiO_2(c) and TiN/N-TiO_2-7 is an indicative of defect sites with a low oxygen coordination (i.e., oxygen vacancies (V_O) or low-valence Ti^{3+}), which would not only regulate the electron distribution to improve the electronic conductivity of TiO_2 [33], but also narrow the bandgap of TiO_2 to endow an enhanced visible-light-responsive activity [11,33,34]. The N 1s spectrum (Fig. 2(d)) of the TiN product delivers a BE peak at 398.1 eV, suggesting the existence of N^{3-}, which can be ascribed to the lattice N of TiN [20], and the N 1s spectrum for TiN/N-TiO_2-7 can be fitted by the two BE peaks at 398.2 and 398.9 eV, ascribable to the N–Ti bond in the TiN phase and the N–Ti–O bond in the N-TiO_2 [35], respectively. The Ti 2p peak of TiN/N-TiO_2 shifts approximately 0.3 eV toward the higher BE one compared with the TiO_2(c), while the Ti 2p peak of TiN/N-TiO_2 shift approximately 0.4 eV toward the lower BE one compared with the TiN (Fig. 2(b)). These BE peak shifts and the presences of N–Ti–O/Ti–N–O linkages suggest that the *in situ* formed TiN and N-TiO_2 components have a strong electron donor-acceptor

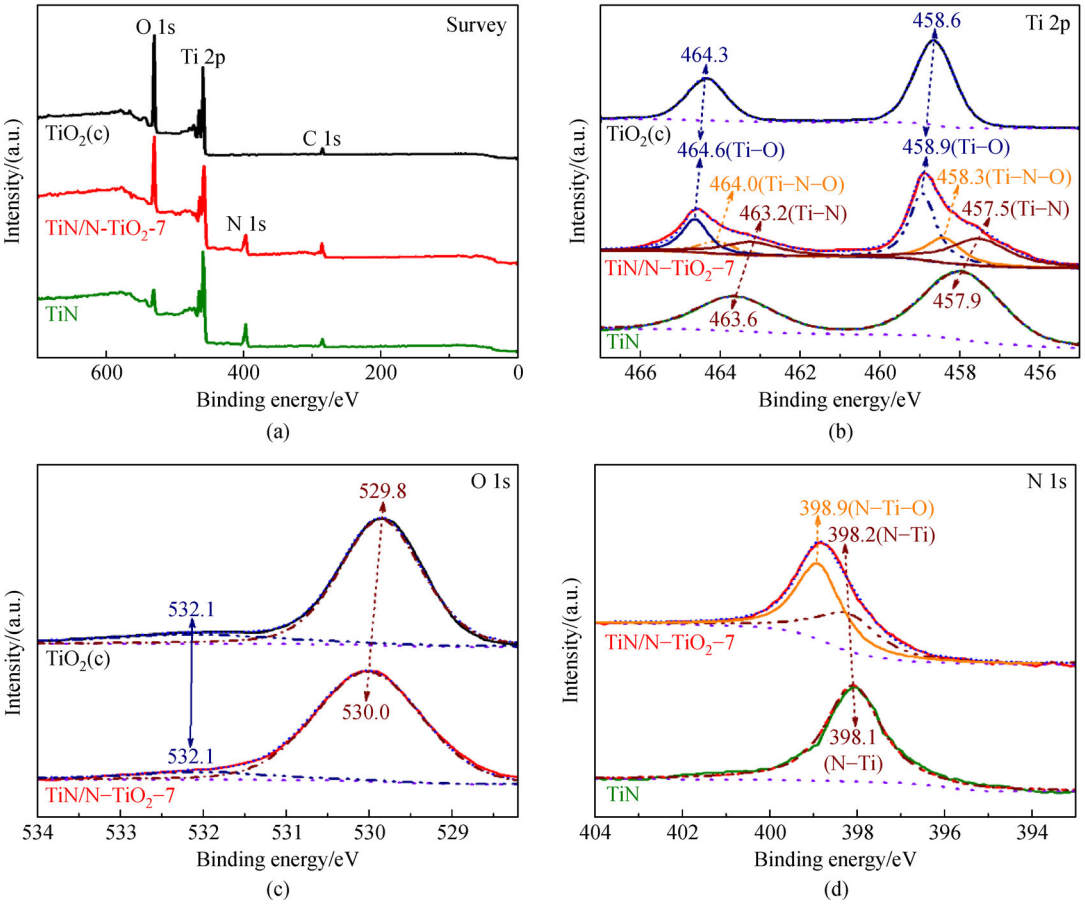

Fig. 2 XPS spectra of the TiO_2(c), TiN, and TiN/N-TiO_2-7 composite derived from TiO_2/MA mass ratio of 1:7. (a) Survey spectra; (b) high-resolution Ti 2p spectra; (c) high-resolution O 1s spectra; (d) high-resolution N 1s spectra.

coupling. Although it was reported that the pyrolysis of MA at 450°C – 500°C can produce g-C_3N_4 [9], the N 1s regional spectra of TiN and TiN/N-TiO_2-7 (Fig. 2(d)) do not display any BE peak (at above 398.9 eV) that can be ascribable to the N atoms bonded to the C atom (C = N–C) and N-(C_3) groups of g-C_3N_4 [9]. This implies that TiN and TiN/N-TiO_2-7 have no coexisted g-C_3N_4, which is reasonable considering the fact that the present products were calcined at 750°C and the thermal decomposition temperature of g-C_3N_4 is in the range of 450°C – 630°C [9].

According to the SEM and TEM images (Figs. 3(a) and 3(b)), the TiO_2(c) product has nanorod-like morphology, and the lattice fringes (approximately 0.357 nm) in the HRTEM image with the corresponding fast Fourier transform (FFT) pattern (Fig. 3(c) and the inset) indicate that anatase TiO_2 is the main component in the TiO_2(c) product. From the SEM and TEM images (Figs. 3(d) and 3(e)) of TiN/N-TiO_2-5 composite, it can be found that those newly formed nanoparticles closely contact on the nanorods, and the HRTEM image (Fig. 3(f) and the insets)

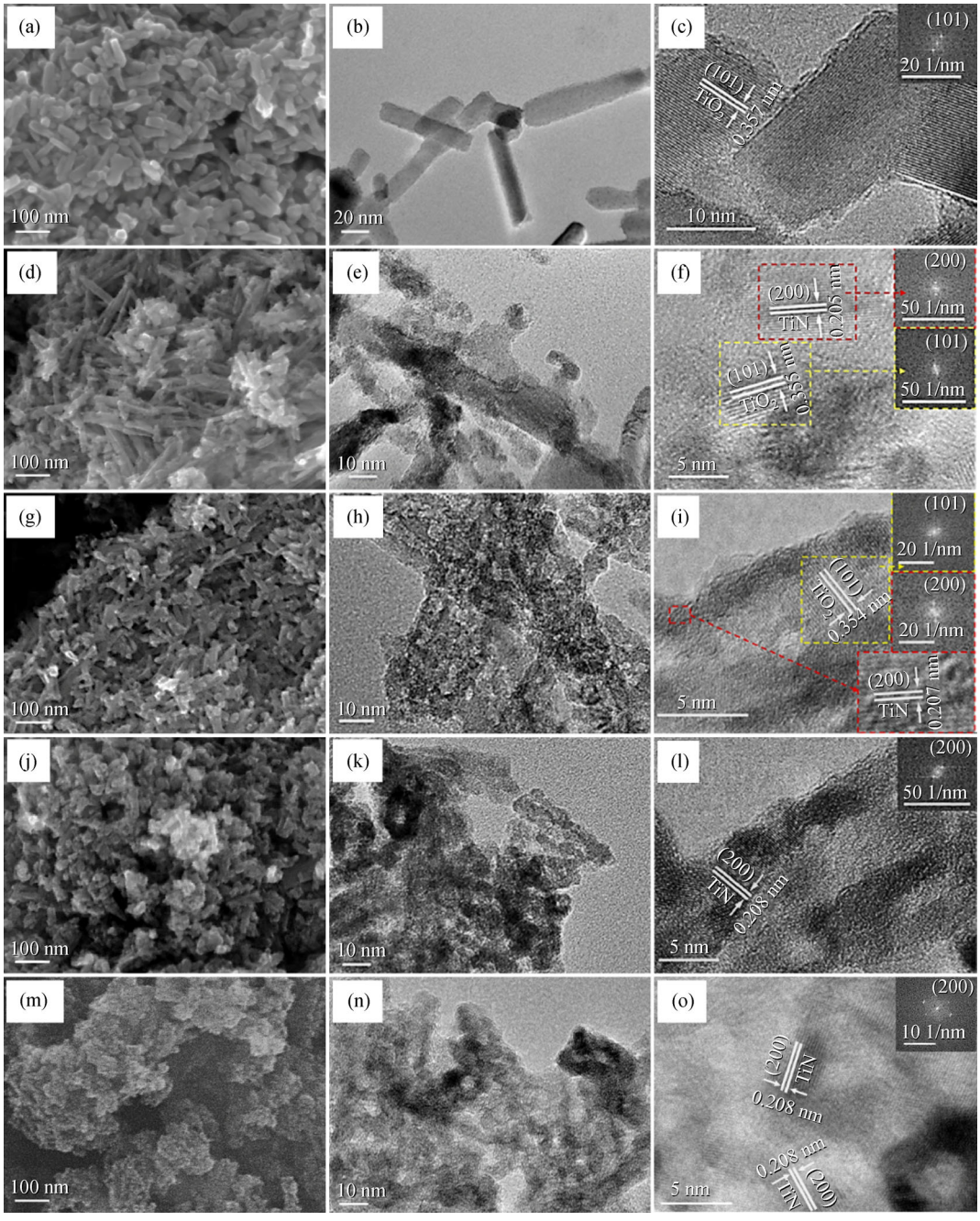

Fig. 3 FESEM, TEM and HRTEM images.
(a–c) TiO_2(c); (d–f) TiN/N-TiO_2-5; (g–i) TiN/N-TiO_2-7; (j–l) TiN/N-TiO_2-10; (m–n) TiN (FESEM (a, d, g, j, and m), TEM (b, e, h, k, and n), and HRTEM (c, f, i, l, and o) images).

displays two kind of lattice fringes of approximately 0.354 and approximately 0.207 nm, which can be attributed to the *d*-spacing of anatase TiO_2 (101) and TiN (200) facets according to their respective FFT patterns, respectively. This observation combined with the above XRD and XPS analysis results demonstrate that TiN nanoparticles gradually formed on those nanorod surface.

Along with the increase of the TiO_2 to MA mass ratio of 1:7 and 1:10, the corresponding composites (TiN/N-TiO_2-7 and TiN/N-TiO_2-10) changed into a more obvious mixed morphology with more TiN nanoparticles intimately attached on TiO_2 nanorods (Figs. 3(g)–3(l)). When the TiO_2 to MA mass ratio is 1:10, the resultant TiN/N-TiO_2-10 displays an amorphous-like morphology (Figs. 3(j) and 3(k)), and the lattice fringes are mainly TiN with a *d*-spacing of 0.208 nm (Fig. 3(l)). Once the TiO_2/MA mass ratio is enhanced to 1:20, the corresponding TiN product changes into amorphous-like nanoparticle agglomerates with not any nanorod-like morphology (Figs. 3(m) and 3(n)), and only lattice fringes (with a *d*-spacing of 0.208 nm) of TiN can be observed (Fig. 3(o)). This implies that the *in situ* nitridation process in the presence of MA leads to the change of the TiO_2 morphology, and thus those nanoparticles attached on nanorods shown in Figs. 3(d)–3(l) can be attributed to TiN. In addition, the elemental analysis results indicate that the TiN/N-TiO_2-10 still contains certain amount of TiO_2 (Table 1), and the O content in those TiN/TiO_2 composites gradually reduce along with the increase of N contents upon enhancing the MA addition amount. This indicates that the oxygen atoms in TiO_2 were successfully substituted with nitrogen atoms to form N-TiO_2 and even TiN (whose amount is gradually increased). These results are well consistent with the above results on the XRD patterns and XPS spectra, from which the slight shifts of the diffraction peaks of anatase TiO_2 (Fig. 1(b)) and the presences of N–Ti–O/Ti–N–O linkages (Figs. 2(b) and 2(d)) can be observed from those composites. Therefore, it can be concluded that the TiN decorated N-TiO_2 composite with intimate interface contact can be fabricated via the *in situ* nitridation process, which will be beneficial for extending the spectral response range and accelerating the photoexcited charge transfer, and then enhancing the photocatalytic H_2 evolution as discussed below.

3.2 Photocatalytic H_2 evolution performance analysis

By using the TiN/N-TiO_2-7 composite as photocatalyst, control experiments were conducted to optimize the photoreaction condition. It was found that an optimal condition (30 mg of 2% (mass fraction) Pt-loaded photocatalyst dispersed in a 50 mL of sacrificial agent aqueous solution) can deliver the best photocatalytic performance under illumination of full spectrum of 300 W Xe-lamp. Among those used electron donors including 10% (volume fraction) triethanolamine (TEOA), 50 mmol/L ascorbic acid (AA), 10 mmol/L disodium ethylenediamine tetraacetic acid (EDTA), 10% (volume fraction) methanol (CH_3OH) and Na_2S (0.35 mol/L) + Na_2SO_3 (0.25 mol/L) solution (Fig. 4(a)), AA can enable the best H_2 evolution activity (453 μmol/h). Besides, the activity of the reaction system containing AA can be further improved by adjusting the pH value using the diluent HCl or NaOH solution (Fig. 4(b)). When the pH value is enhanced from 1.0 to 3.0, the H_2 evolution activity displays an increasing trend, and the activity reaches up to 703 μmol/h when the pH value is 3.0. Further enhancing the pH to higher than 3.0, the H_2 evolution rate was remarkably reduced, which might be caused by the decreased electron-donor capacity of AA in a photoreaction system with $pH > 3.0$ [36].

Based on the optimized condition, control experiments were also conducted to optimize the TiO_2 to MA mass ratio during the *in situ* nitridation process of the hydrothermally synthesized TiO_2. As depicted in Fig. 4(c), all those composites (TiN/N-TiO_2-5, TiN/N-TiO_2-7, and TiN/N-TiO_2-10) exhibit a much higher H_2 evolution activity than the single TiO_2(c) and TiN illuminated with full spectrum of 300 W Xe-lamp, which can be ascribed to the close contacted TiN to N-TiO_2 components to significantly retard the photogenerated charge carrier recombination. Especially, the TiN/N-TiO_2-7 delivers the maximum H_2 evolution activity (703 μmol/h), which is approximately 2.6 and 32.0 times more than that of TiO_2 (270 μmol/h) and TiN (22 μmol/h) alone, respectively. Under visible light ($\lambda > 400$ nm) illumination, the single TiO_2(c) and TiN show a very limited photoactivity, but the TiN/N-TiO_2-7 still shows the best H_2 evolution activity (368 μmol/h), much higher than that (285 μmol/h) of

Table 1 Composition and bandgap of TiO_2(c), TiN, and their composites derived from different TiO_2/MA mass ratios

Sample	Ti/mol%	O/mol%	N/mol%	Ti/O molar ratio	Ti/N molar ratio	TiN/TiO_2 molar ratio	Bandgap/eV
TiO_2(c)	33.2	66.8	–	1:2.01	–	–	3.16
TiN/N-TiO_2-5	35.4	49.2	10.8	1:1.39	1:0.31	1:2.28	2.96
TiN/N-TiO_2-7	37.7	39.6	17.8	1:1.05	1:0.47	1:1.12	2.76
TiN/N-TiO_2-10	39.8	30.2	24.6	1:0.76	1:0.62	1:0.62	2.71
TiN	47.6	3.52	44.1	1:0.07	1:0.93	1:0.08	–

TiN/N-TiO_2-5. In addition, the recycling stability experiment for H_2 generation over the TiN/N-TiO_2-7 was conducted for three cycles, whereby the photoreaction system was evacuated thoroughly and then irradiated with the full spectrum of the 300 W Xe-lamp. After each cycle, the photocatalyst was repetitively washed with deionized water and alcohol for several times, then dried under vacuum. As seen, an average H_2 evolution activity of 655 μmol/h is obtained in the first run of 3 h under 300 W Xe-lamp irradiation, and the activity remains 90% at the last run (Fig. 4(f)). The slight reduction in the activity may stem from the attachment of decomposed product of AA on the photocatalyst. The above results demonstrate that the TiN/N-TiO_2-7 possesses a superior H_2 evolution activity and a relatively good stability under the above optimized condition.

3.3 Energy band and photocatalytic mechanism analysis

To explore the underlying photocatalytic mechanism of the TiN/N-TiO_2 composite, its optical absorption property and energy band structure are investigated. Figure 5(a) displays the UV-vis diffuse reflectance absorption spectra (DRS). As shown, the TiO_2(c) product exhibits a narrow UV-light absorption range with an onset absorption edge at 393.2 nm, corresponding to the bandgap of 3.16 eV, which is similar to that in Refs. [37,38]. On the contrary, the TiN obtained from the TiO_2 to MA mass ratio of 1:20 exhibits a very broad spectral absorption range with an enhanced visible light absorption in the range of 400 – 800 nm, which is resulted from the plasmonic absorption of TiN [20,21]. Usually, TiN exhibits a broader plasmonic absorption peak ranging from 450 to 850 nm, further compared with the plasmonic noble metal (e.g. Au) nanoparticles [21]. As for those TiN/N-TiO_2 composites, the absorption edges are extended to the visible region due to the nitrogen incorporation into the TiO_2 lattice, whose absorption intensity elevates gradually with increasing the TiO_2 to MA mass ratio, and then cause the corresponding bandgap to decrease (Table 1). Especially, the absorption edge of TiN/N-TiO_2-10 can be extended to approximately 485.0 nm. This extended spectral absorption is in good consistent with the N-TiO_2 reported previously [39]. More importantly, those TiN/N-TiO_2 composites display an additional visible absorption in the range of 450–900 nm, which is very similar to that of the TiN/N-TiO_2

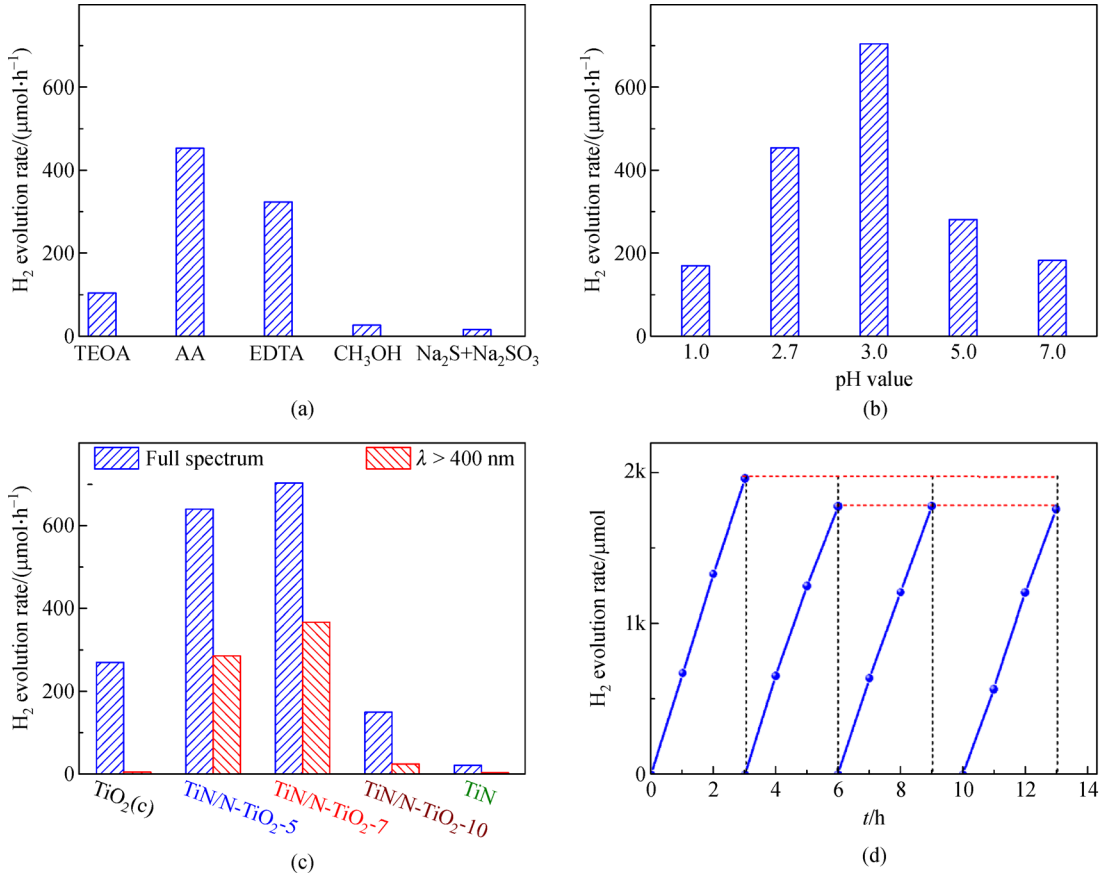

Fig. 4 Effects of reaction conditions on the photoactivity and time course of the H_2 production.
(a) Sacrificial reagent; (b) pH value of AA solution; (c) TiO_2/MA mass ratio; (d) time course of the H_2 production over the TiN/N-TiO_2-7 composite under the optimized photoreaction condition (All are under Xe-lamp full spectrum illumination, and the situation under visible light ($\lambda > 400$ nm) illumination is also listed in (c)).

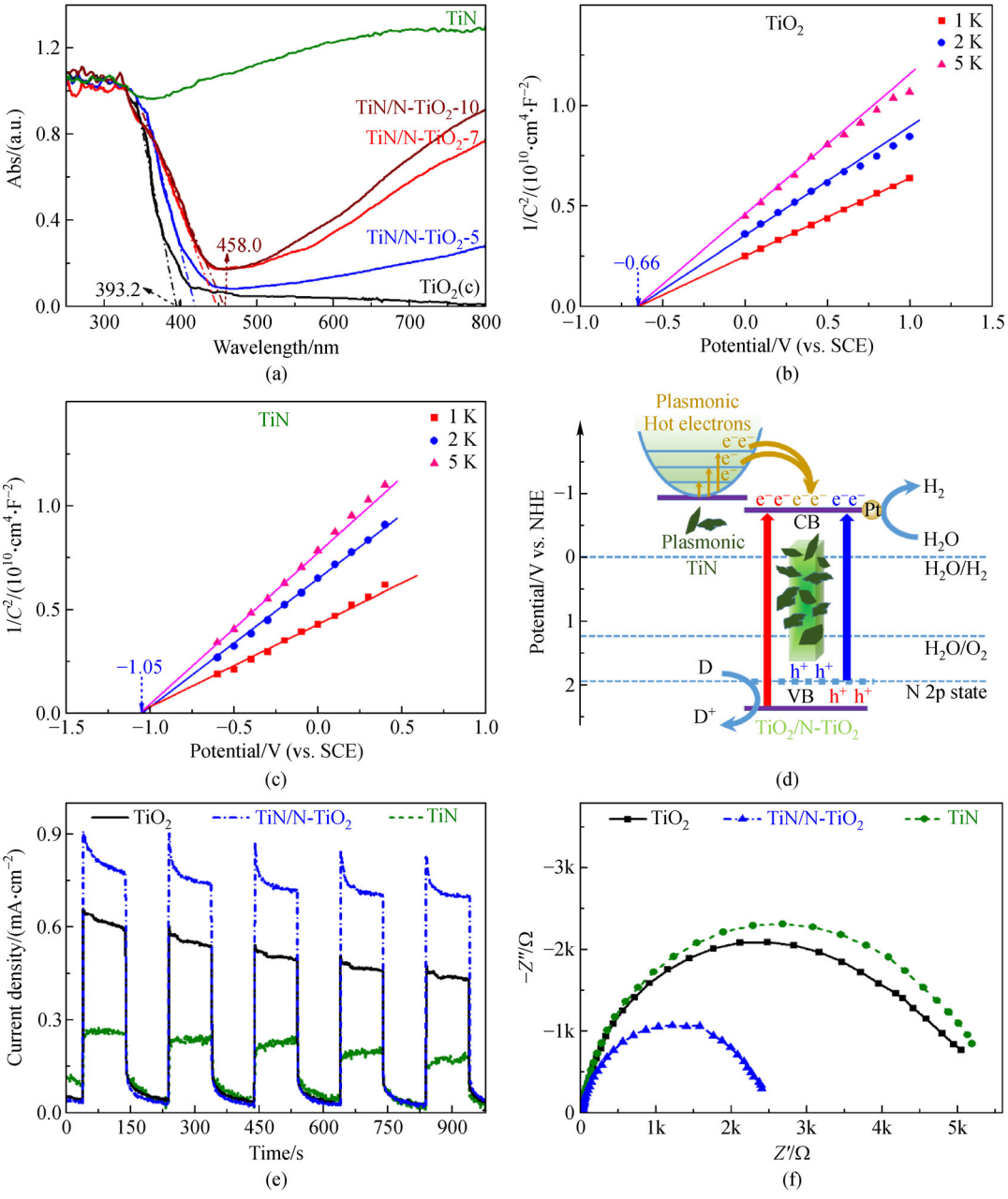

Fig. 5 Energy band structures and (photo)electrochemical performance.

(a) DRS spectra of the TiO_2, TiN, and their composites (TiN/N-TiO_2) derived from various TiO_2/MA mass ratios; (b) Mott-Schottky plots of the TiO_2 film obtained at a frequency of 1, 5, or 10 kHz in Na_2SO_4 solution (1.0 mol/L); (c) Mott-Schottky plots of the TiN film obtained at a frequency of 1, 5, or 10 kHz in Na_2SO_4 solution (1.0 mol/L); (d) schematic mechanism of the TiN/N-TiO_2 composite boosting the H_2 evolution activity; (e) photocurrent-time curves of the TiO_2, TiN, and TiN/N-TiO_2 composite derived from TiO_2/MA mass ratio of 1:7; (f) Nyquist plots of the TiO_2, TiN, and TiN/N-TiO_2 composite derived from TiO_2/MA mass ratio of 1:7.

reported previously [20], and thus can be ascribed to the plasmonic effect of the co-existed TiN in the present composite [20,21]. Due to the localized surface plasmon resonance of TiN, a strong electric field is formed at the TiN/N-TiO_2 interface, which enhances the visible light absorption in the range of 600–900 nm and the photoelectrochemical oxygen evolution performance of the composite [20]. Similarly, it can be concluded that the coexistence of TiN will be conducive to the utilization of visible light, and resulting in the superior H_2 evolution performance of the present TiN/N-TiO_2 composite under UV–vis light.

The Mott-Schottky plots (Fig. 5(b)) were employed to determine the E_{fb} of TiO_2(c), and the positive slope denotes that TiO_2(c) is an n-type semiconductor. All Mott-Schottky plots of the TiO_2(c) film have the same intercept with the x-axis at −0.66 V versus SCE (E^{θ} = 0.24 V versus NHE)

[40,41], and thus its flat-band potential (E_{fb}) can be calculated to be -0.66 V + 0.24 V = -0.42 V versus NHE. Since the conduction band (CB) bottom is more negative by approximately -0.1 V than E_{fb} for a certain n-type semiconductor [42], the CB level (E_{CB}) of TiO_2(c) can be estimated to be approximately -0.52 V versus NHE. According to Fig. 5(a) and Table 1, the E_g value of TiO_2(c) is 3.16 eV, thus, its valence band (VB) level (E_{VB}) can be calculated to be 2.64 V versus NHE according to the formula ($E_{VB} = E_g + E_{CB}$). Similarly, the Mott-Schottky plots (Fig. 5(c)) of the TiN film indicate that the E_{fb} is $-1.05 + 0.24 = -0.81$ V versus NHE, corresponding a work function of 3.93 (= –0.81 + 4.74) eV versus vacuum, similar to the reported value (approximately 4.0 eV) [23]. According to the above results, the energetic alignment of the TiN/N-TiO_2 composite (derived from the TiO_2 to MA mass ratio of 1:7) can be drown as shown in Fig. 5(d). Under full spectrum illumination of the Xe-lamp, the TiN/N-TiO_2 composite enables a broad UV-vis light photon capturing by the nitrogen-doping and the plasmonic effect of the *in situ* formed TiN. The E_{CB} level of N-TiO_2 is negative compared to the H^+/H_2 reduction potential (E = –0.0592pH = $-$ 0.18 V versus NHE) since the pH value of photoreaction suspension is 3.0 (Fig. 4(b)), while the E_{fb} (-0.81 V) of TiN is negative compared to the E_{CB} (–0.52 V) of N-TiO_2. This energetic alignment is thermodynamically favorable for hot carrier injecting to the CB of N-TiO_2 [21], and those injected electrons and the photoexcited ones of N-TiO_2 are further transferred to the Pt cocatalyst to participate in the H_2 evolution reaction [43,44]. Meanwhile, the photogenerated holes remain in N-TiO_2 transfer to the photocatalyst for the oxidation reaction of hole scavenger [45].

To further confirm the above mechanism, the transient photocurrent response and the electrochemical impedance spectra (EIS) of the TiO_2(c), TiN, and TiN/N-TiO_2 composite (derived from the TiO_2 to MA mass ratio of 1:7) were also conducted. As shown in Fig. 5(e), the TiN/N-TiO_2 composite displays the largest photocurrent among the three materials, demonstrating that the composite has more efficient charge transfer/separation processes. Additionally, the smaller radius (Fig. 5(f)) of the TiN/N-TiO_2 composite than the TiN and TiO_2(c) alone indicates the lower interfacial resistance, which is consistent with the superior photocatalytic performance. As mentioned above, TiN/N-TiO_2-7 still shows the best H_2 evolution activity (368 μmol/h) under visible light illumination (Fig. 4(c)). However, there is no obvious H_2 evolved over the single TiN and TiO_2(c). It is reasonable to consider that the TiO_2(c) has a wide bandgap as shown in Fig. 5(a). As for the single plasmonic TiN, it covers a wider wavelength range of the solar spectrum (Fig. 5(a)), enabling a more efficient and broadband hot carrier generation [21], and its limited activity (Fig. 4(c)) may be caused by the rapid recombination of those broadband-derived hot carriers of TiN, which can be demonstrated by the very low photocurrent and larger interfacial resistance (Fig. 5(e) and 5(f)). The reason for the obviously enhanced activity of those composites is that the coexisting N-TiO_2 can accept the hot electrons of TiN and then transfer them to Pt for H_2 evolution reaction. Based on the above results and discussion, it can be concluded that the high visible light utilization stemming from both the N-doping and the plasmonic effect of TiN, the well-aligned energy band structure and intimate interfacial contact between TiN and N-TiO_2 facilitate the generation, transfer, and separation of photoinduced charge (and hot charge) carriers, thus boosting the photocatalytic H_2 generation performance of TiN/N-TiO_2 composite.

4 Conclusions

In summary, a nonmetallic plasmonic TiN decorated N-doped titania (N-TiO_2) composite (TiN/N-TiO_2) was fabricated via an *in situ* nitridation of hydrothermally synthesized TiO_2, and the TiN was *in situ* grown on the formed N-TiO_2 with an intimate contact interface. The resultant TiN/N-TiO_2 composite was characterized with various techniques to explore the crystal phase, morphology, microstructure, chemical composition/states, and energy band structure. The *in situ* formed plasmonic TiN and N-TiO_2 can extend the spectral response range of TiO_2 and promote the hot charge carrier separation of TiN via the close contact interface, therefore delivering a highly efficient H_2 evolution activity (703 μmol/h), which is approximately 2.6 and 32.0 times more than that of TiO_2 and TiN alone under the irradiation of full spectrum of the 300 W Xe-lamp, respectively. This work provides a fascinating approach to *in situ* formation of nonmetallic plasmonic material/N-TiO_2 composite photocatalysts for high-efficiency photocatalytic H_2 evolution.

Acknowledgements This work was supported by the National Natural Science Foundation of China (Grant Nos. 21975190, 21573166, and 21271146), the Science and Technology Program of Science, Technology and Innovation Commission of Shenzhen Municipality (JCYJ20180302-153921190), and the Funds for Creative Research Groups of Hubei Province (2014CFA007), China.

References

1. Fujishima A, Honda K. Electrochemical photolysis of water at a semiconductor electrode. Nature, 1972, 238(5358): 37–38
2. Wang Q, Nakabayashi M, Hisatomi T, et al. Oxysulfide photocatalyst for visible-light-driven overall water splitting. Nature Materials, 2019, 18(8): 827–832
3. Wang J M, Luo J, Liu D, et al. One-pot solvothermal synthesis of MoS_2-modified $Mn_{0.2}Cd_{0.8}S$/MnS heterojunction photocatalysts for highly efficient visible-light-driven H_2 production. Applied Catalysis B: Environmental, 2019, 241: 130–140
4. Chen X P, Xiong J H, Shi J M, et al. Roles of various Ni species on

TiO_2 in enhancing photocatalytic H_2 evolution. Frontiers in Energy, 2019, 13(4): 684–690

5. Zhang X H, Peng T Y, Song S S. Recent advances in dye-sensitized semiconductor systems for photocatalytic hydrogen production. Journal of Materials Chemistry A, Materials for Energy and Sustainability, 2016, 4(7): 2365–2402
6. Wang J W, Kuo M T, Zeng P, et al. Few-layer $BiVO_4$ nanosheets decorated with $SrTiO_3$: Rh nanoparticles for highly efficient visible-light-driven overall water splitting. Applied Catalysis B: Environmental, 2020, 279: 119377
7. Qu W, Pan J Q, Liu Y Y, et al. Two-dimensional ultrathin MoS_2-modified black Ti^{3+}-TiO_2 nanotubes for enhanced photocatalytic water splitting hydrogen production. Journal of Energy Chemistry, 2020, 43: 188–194
8. Ravi P, Navakoteswara Rao V, Shankar M V, et al. CuO-Cr_2O_3 core-shell structured co-catalysts on TiO_2 for efficient photocatalytic water splitting using direct solar light. International Journal of Hydrogen Energy, 2018, 43(8): 3976–3987
9. Liu D, Zhang S, Wang J M, et al. Direct Z-scheme 2D/2D photocatalyst based on ultrathin g-C_3N_4 and WO_3 nanosheets for efficient visible-light-driven H_2 generation. ACS Applied Materials & Interfaces, 2019, 11(31): 27913–27923
10. Sotelo-Vazquez C, Quesada-Cabrera R, Ling M, et al. Evidence and effect of photogenerated charge transfer for enhanced photocatalysis in WO_3/TiO_2 heterojunction films: a computational and experimental study. Advanced Functional Materials, 2017, 27(18): 1605413
11. Meng S G, Sun W T, Zhang S J, et al. Insight into the transfer mechanism of photogenerated carriers for WO_3/TiO_2 heterojunction photocatalysts: is it the transfer of band-band or Z-scheme? Why? Journal of Physical Chemistry C, 2018, 122(46): 26326–26336
12. Li J, Zhang M, Li X, et al. Effect of the calcination temperature on the visible light photocatalytic activity of direct contact Z-scheme g-C_3N_4-TiO_2 heterojunction. Applied Catalysis B: Environmental, 2017, 212: 106–114
13. Zhuang C S, Wang J M, Zhou S Y, et al. Ruthenium(II) pincer complex bearing N′NN′- and ONO-type ligands as a titania sensitizer for efficient and stable visible-light-driven hydrogen production. ChemPhotoChem, 2018, 2: 765–772
14. He Y M, Dai X Q, Ma S N, et al. Hydrothermal preparation of carbon modified KNb_3O_8 nanosheets for efficient photocatalytic H_2 evolution. Ceramics International, 2020, 46(8): 11421–11426
15. Chen P F, Chen L, Ge S F, et al. Microwave heating preparation of phosphorus doped g-C_3N_4 and its enhanced performance for photocatalytic H_2 evolution in the help of Ag_3PO_4 nanoparticles. International Journal of Hydrogen Energy, 2020, 45(28): 14354–14367
16. Zhang Q L, Chen P F, Chen L, et al. Facile fabrication of novel Ag_2S/K-g-C_3N_4 composite and its enhanced performance in photocatalytic H_2 evolution. Journal of Colloid and Interface Science, 2020, 568: 117–129
17. Chen P F, Dai X Q, Xing P X, et al. Microwave heating assisted synthesis of novel SnSe/g-C_3N_4 composites for effective photocatalytic H_2 production. Journal of Industrial and Engineering Chemistry, 2019, 80: 74–82
18. Cui Z, Zu C, Zhou W, Manthiram A, et al. Mesoporous titanium nitride-enabled highly stable lithium-sulfur batteries. Advanced Materials, 2016, 28(32): 6926–6931
19. Xie Y, Xia C, Du H, et al. Enhanced electrochemical performance of polyaniline/carbon/titanium nitride nanowire array for flexible supercapacitor. Journal of Power Sources, 2015, 286: 561–570
20. Li Y Y, Wang J G, Fan Y C, et al. Plasmonic TiN boosting nitrogen-doped TiO_2 for ultrahigh efficient photoelectrochemical oxygen evolution. Applied Catalysis B: Environmental, 2019, 246: 21–29
21. Naldoni A, Guler U, Wang Z, et al. Broadband hot-electron collection for solar water splitting with plasmonic titanium nitride. Advanced Optical Materials, 2017, 5(15): 1601031–1601041
22. Chirumamilla M, Chirumamilla A, Yang Y, et al. Large-area ultrabroadband absorber for solar thermophotovoltaics based on 3D titanium nitride nanopillars. Advanced Optical Materials, 2017, 5 (22): 1700552
23. Fillot F, Morel T, Minoret S, et al. Investigations of titanium nitride as metal gate, elaborated by metal organic atomic layer deposition using TDMAT and NH_3. Microelectronic Engineering, 2005, 82(3–4): 248–253
24. Fan K, Chen J N, Yang F, et al. Self-organized film of ultra-fine TiO_2 nanotubes and its application to dye-sensitized solar cells on a flexible Ti-foil substrate. Journal of Materials Chemistry, 2012, 22(11): 4681–4686
25. Bakardjieva S, Šubrt J, Štengl V, et al. Photoactivity of anatase-rutile TiO_2 nanocrystalline mixtures obtained by heat treatment of homogeneously precipitated anatase. Applied Catalysis B: Environmental, 2005, 58(3–4): 193–202
26. Zhang X H, Peng T Y, Yu L J, et al. Visible/near-infrared-light-induced H_2 production over g-C_3N_4 co-sensitized by organic dye and Zinc phthalocyanine derivative. ACS Catalysis, 2015, 5(2): 504–510
27. Yu W L, Zhang S, Chen J X, et al. Biomimetic Z-scheme photocatalyst with a tandem solid-state electron flow catalyzing H_2 evolution. Journal of Materials Chemistry A, Materials for Energy and Sustainability, 2018, 6(32): 15668–15674
28. Deb A K, Chatterjee P. Microstrain and lattice disorder in nanocrystalline titanium dioxide prepared by chemical route and its relation with phase transformation. Journal of Theoretical and Applied Physics, 2020, 14(3): 285–293
29. Chen S Y, Gao H Y, Han M Y, et al. *In-situ* self-transformation synthesis of N-doped carbon coating paragenetic anatase/rutile heterostructure with enhanced photocatalytic CO_2 reduction activity. ChemCatChem, 2020, 12(12): 3274–3284
30. Li K, Peng T Y, Ying Z H, et al. Ag-loading on brookite TiO_2 quasi nanocubes with exposed {210} and {001} facets: activity and selectivity of CO_2 photoreduction to CO/CH_4. Applied Catalysis B: Environmental, 2016, 180: 130–138
31. Clatworthy E B, Yick S, Murdock A T, et al. Enhanced photocatalytic hydrogen evolution with TiO_2-TiN nanoparticle composites. Journal of Physical Chemistry C, 2019, 123(6): 3740–3749
32. Kang C, Xiao K K, Wang Y H, et al. Synthesis of $SrTiO_3$-TiN nanocomposites with enhanced photocatalytic activity under simulated solar irradiation. Industrial & Engineering Chemistry Research, 2018, 57(34): 11526–11534

33. Wang Z, Yang C, Lin T, et al. Visible-light photocatalytic, solar thermal and photoelectrochemical properties of aluminium-reduced black titania. Energy & Environmental Science, 2013, 6(10): 3007–3014
34. Naldoni A, Allieta M, Santangelo S, et al. Effect of nature and location of defects on bandgap narrowing in black TiO_2 nanoparticles. Journal of the American Chemical Society, 2012, 134(18): 7600–7603
35. Li L, Zhang X, Wu G, et al. Supercapacitor electrodes based on hierarchical mesoporous MnO_x/nitrided TiO_2 nanorod arrays on carbon fiber paper. Advanced Materials Interfaces, 2015, 2(6): 1400446
36. Han Z J, Qiu F, Eisenberg R, et al. Robust photogeneration of H_2 in water using semiconductor nanocrystals and a nickel catalyst. Science, 2012, 338(6112): 1321–1324
37. Khan S U M, Al-Shahry M, Ingler W B. Efficient photochemical water splitting by a chemically modified n-TiO_2. Science, 2002, 297 (5590): 2243–2245
38. Kumar S G, Devi L G. Review on modified TiO_2 photocatalysis under UV/visible light: selected results and related mechanisms on interfacial charge carrier transfer dynamics. Journal of Physical Chemistry A, 2011, 115(46): 13211–13241
39. Wang G, Xiao X, Li W, et al. Significantly enhanced visible light photoelectrochemical activity in TiO_2 nanowire arrays by nitrogen implantation. Nano Letters, 2015, 15(7): 4692–4698
40. Han L L, Song S Y, Liu M J, et al. Stable and efficient single-atom Zn catalyst for CO_2 reduction to CH_4. Journal of the American Chemical Society, 2020, 142(29): 12563–12567
41. Wang J, Zhao J, Yang J, et al. An electrochemical sensor based on MOF-derived NiO@ZnO hollow microspheres for isoniazid determination. Mikrochimica Acta, 2020, 187(7): 380
42. Grubač Z, Katić J, Metikoš-Huković M. Energy-band structure as basis for semiconductor n-Bi_2S_3/n-Bi_2O_3 photocatalyst design. Journal of the Electrochemical Society, 2019, 166(10): H433
43. Huang X Y, Liu Y Y, Wen H, et al. Ensemble-boosting effect of Ru-Cu alloy on catalytic activity towards hydrogen evolution in ammonia borane hydrolysis. Applied Catalysis B: Environmental, 2021, 287: 119960
44. Liu Y Y, Wen H, Zhou D J, et al. Tuning surface *d* charge of Ni-Ru alloys for unprecedented catalytic activity towards hydrogen generation from ammonia borane hydrolysis. Applied Catalysis B: Environmental, 2021, 291: 120094
45. Wang J M, Xu L, Wang T X, et al. Porphyrin conjugated polymer with periodic type II-like heterojunctions and single-atom catalytic sites for broadband-responsive hydrogen evolution. Advanced Functional Materials, 2021, 31(16): 2009819